Core−Shell Ellipsoidal MnCo$_2$O$_4$ Anode with Micro-/Nano-Structure and Concentration Gradient for Lithium-Ion Batteries

Guoyong Huang,[†] Shengming Xu,[*,†,‡] Zhenghe Xu,[*,†,§] Hongyu Sun,[‖] and Linyan Li[†]

[†]Institute of Nuclear and New Energy Technology, Tsinghua University, Beijing 100084, China

[‡]Beijing Key Lab of Fine Ceramics, Tsinghua University, Beijing 100084, China

[§]Department of Chemical and Materials Engineering, University of Alberta, Edmonton, Alberta T6G 2V4, Canada

[‖]Beijing National Center for Electron Microscopy, School of Materials Science and Engineering, Tsinghua University, Beijing 100084, China

S *Supporting Information*

ABSTRACT: In this study, novel core−shell ellipsoidal MnCo$_2$O$_4$ powders with desired micro/nano-structure and a unique concentration gradient have been synthesized as anode material for Li-ion batteries. The special porous ellipsoid (2.5−4.5 μm in the long axis, 1.5−2.5 μm in the short axis, 200−300 nm in the thickness of shell) is built up by irregular nanoparticles attached to each other, and corresponding to the ellipsoid with concentration gradient, the Co/Mn atomic ratios of core and shell are about 1.76:1 and 2.34:1, respectively. The good performance, including high initial discharge capacities (1433.3 mAhg^{-1} at 0.1 Ag^{-1} and 1248.4 mAhg^{-1} at 0.4 Ag^{-1}), advanced capacity retention (∼900.0 mAhg^{-1} after 60 cycles at 0.1 Ag^{-1}), and fair rate performance (∼620.0 mAhg^{-1} after 50 cycles at 0.4 Ag^{-1}) has been measured by the battery test. Remarkably, the ellipsoidal shape and core−shell microstructure with concentration gradient are still maintained after 70 cycles of charge/discharge at 0.1 Ag^{-1}.

KEYWORDS: *MnCo$_2$O$_4$, core−shell, ellipsoidal, micro/nano-structure, concentration gradient, electrochemistry*
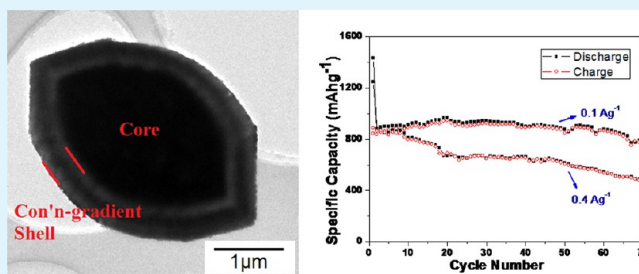
INTRODUCTION

Decreasing availability of fossil fuels and climate change force us to develop sustainable and renewable energy conversions and electrical energy storage systems, such as Li-ion batteries (LIBs) and supercapacitors (SCs).[1,2] Despite tremendous research efforts that led to great advances in developing high performance LIBs, the performance of LIBs still needs substantial improvement before they can be widely accepted for future applications ranging from portable electronics to electric vehicles (EVs) and hybrid electric vehicles (HEVs) to the energy source of large industrial equipment.[3,4] Developing electrode materials is a key element to achieve the required performance and capacity of LIBs for these important applications. Transition metal oxides (e.g., Co$_3$O$_4$,[5] CoO,[6] NiO,[7] CuO,[8] Mn$_3$O$_4$,[9] TiO$_2$,[10,11] and so on) and their composites (e.g., CoO/graphene[12] and Mn$_3$O$_4$/graphene[13]) have been considered as promising anode materials owing to their high theoretical capacities and good cycling stability.[14−17] Remarkably, spinel binary transition-metal oxides, AB$_2$O$_4$ (e.g., NiCo$_2$O$_4$,[18,19] NiFe$_2$O$_4$,[20] CoFe$_2$O$_4$,[21] ZnCo$_2$O$_4$,[22,23] MnCo$_2$O$_4$,[24,25] CoMn$_2$O$_4$,[26] and so on), and their composites (e.g., NiCo$_2$O$_4$/graphene[27] and NiCo$_2$O$_4$/Carbon[28]) have been widely investigated because of the lower cost and better electronic conductivity than the single-metal oxides.[29,30] Among them, the electrochemical performance of MnCo$_2$O$_4$

could be enhanced by the complementarity and synergy of Co and Mn in the charge/discharge process.[31] For example, hollow MnCo$_2$O$_4$ submicrospheres show a large initial charge capacity of 1119 mAhg^{-1} at 400 mAg^{-1}.[32] MnCo$_2$O$_4$ nanowire arrays deliver an initial specific discharge capacity of 1288.6 mAhg^{-1} and reversible capacity retention of 92.7% after 50 cycles at 100 mAg^{-1}.[33] These two unique features motivated us to further investigate the electrochemical performance of MnCo$_2$O$_4$ by designing special nano/micro-structures and a desired morphology of MnCo$_2$O$_4$ with a controlled concentration gradient.

As we all know, the microstructure of electronic material is one of the crucial factors to impact its property.[3,34] Micro/nano-structured materials in the form of microscale particles assembled or constructed from nanoscale components can both avoid the shortcomings of nanomaterials and retain them to inherit the advantages. Therefore, the design of micro/nano-structure of microscale particles as building blocks would be a good direction to improve the performance of LIB electrode materials.[35,36] For example, micro/nano-structured Co$_3$O$_4$ cubes consisting of nanosheets show excellent capacity

Scheme 1. Possible Formation Path of the Core−Shell Ellipsoidal MnCo$_2$O$_4$ with Micro-/Nano-Structure and Concentration Gradient
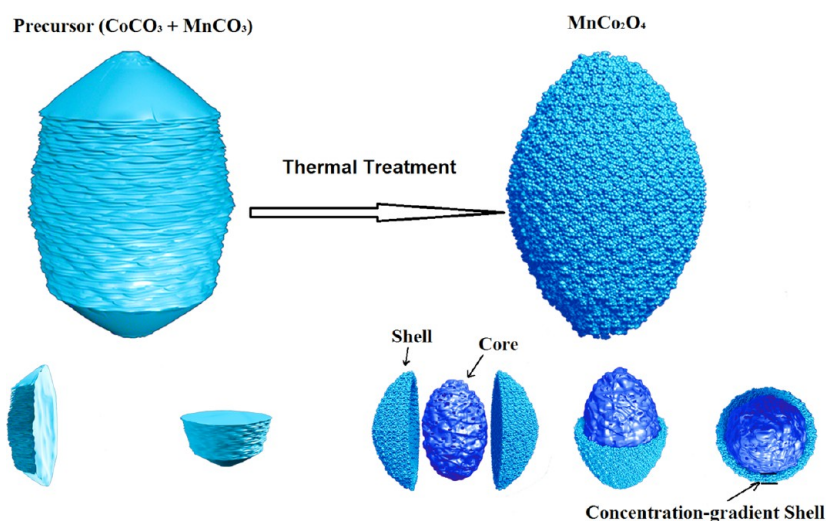
retention of 99.2% and 89.9% after 60 cycles at 0.5 and 1 C, respectively.[37] Nano/submicro-sized CuO powders exhibit a stable capacity of ~620 mAhg^{-1} after 40 cycles at 60 mAg^{-1}.[38] Hierarchical Co$_x$Mn$_{3-x}$O$_4$ arrays with micro/nano-structures show an excellent performance with remarkable specific capacities from 540 to 200 mAhg^{-1} at various current rates (1−10 C).[39] On the other hand, the concentration gradient of electronic materials could enhance the rate capability and the thermal property of batteries.[40,41] For instance, spherical lithium-rich layered Li$_{1.13}$[Mn$_{0.534}$Ni$_{0.233}$Co$_{0.233}$]$_{0.87}$O$_2$ with an outer layer concentration gradient shows excellent lithium intercalation stability with capacity retention at 97.2% after 100 cycles over 0.5 C at 25 °C and an enhanced thermal property with capacity retention of 92.4% after 50 cycles at 55 °C.[42] A core material of Li[Ni$_{0.8}$Co$_{0.2}$]O$_2$ encapsulated completely within a stable manganese-rich concentration-gradient shell delivers a very high capacity of 200 mAhg^{-1} after 50 cycles over 0.2 C at 55 °C.[43] However, very few reports have been published on micro/nano-structured binary transition-metal oxide LIB anode of the concentration gradient.

Herein, a novel core−shell ellipsoidal MnCo$_2$O$_4$ LIB anode material of desired micro/nano-structure and unique concentration gradient was designed and synthesized successfully using a facile hydrothermal method followed by thermal treatment. Due to its special micro/nano-structure and desired concentration gradient in the core−shell ellipsoidal shape, this material exhibited good electrochemical performance.

■ EXPERIMENTAL SECTION

Materials Preparation. All reagents are analytical grade without further purification. Co(CH$_3$COO)$_2$·4H$_2$O (1.660 g), Mn-(CH$_3$COO)$_2$·4H$_2$O (0.817 g), CO(NH$_2$)$_2$ (3.000 g), and (HOCH$_2$CH$_2$)$_3$N (triethanolamine, 2.000 g) were dissolved orderly in deionized water under vigorous stirring to obtain a 100 mL transparent solution. It was then transferred into a Teflon-lined stainless steel autoclave (140 mL), and a thermal treatment was performed for the sealed autoclave in an electric oven at 180 °C for 12 h. After reaction, the pink powders in the autoclave were collected and washed by deionized water and pure ethanol before being dried in a vacuum oven at 60 °C for 24 h. In order to get micro/nano-structured MnCo$_2$O$_4$, another thermal treatment was performed in air at 800 °C for 10 h with a heating ramp of 2 °C·min^{-1}. Then, the black powders were collected for further characterization.

Materials Characterization. The crystal structure was characterized by X-ray powder diffraction (XRD) (Cu Kα radiation, Bruker, D8 Advance). The specific surface area and pore size distribution were calculated by the specific surface area and porosity analyzer (Micromeritics, Gemini VII 2390). The micro morphologies were observed by a scanning electron microscope (SEM) (JEOL, JSM 5500) and transmission electron microscope (TEM) (JEOL, JSM 2011 and FEI, Tecnai G2 F20). To observe the internal morphology and determine the local composition of as-prepared particles directly, a very small amount of MnCo$_2$O$_4$ powders was embedded in an epoxy resin and baked to cure the sample as a block. To optimize cutting results, the resin should have a similar hardness as the MnCo$_2$O$_4$ sample to avoid the particles from being pulled out during the cutting. To make the cutting surface smooth, the epoxy block was trimmed by a diamond knife on an optical microscope under the ultramicrotome (Leica, Lecia EM UC6). After trimming, the block was fixed on the metallic disk mounted on the ultramicrotome for cutting. Surfaces were cut by following the procedures for thin sectioning. Then, the thin sections, which were cut off, were collected to prepare SEM samples. Then, the SEM samples with thin sections were used to characterize the concentration gradients of sections by an energy dispersive X-ray spectrometer (EDX) equipped on the SEM device (JEOL, JSM 5500).

Electrochemical Characterizations. MnCo$_2$O$_4$ (70 mg), acetylene black (ATB) (20 mg), and polytetrafluoroethylene (PTFE) solution (200 mg; the weight percentage is 5%, and the solvent is ethanol) were mixed uniformly. Through the tablet machine, the black mixture was prepared into a piece of thin sheet. Then, the sheet was cut into small disks as electrodes (5 mm in diameter) by a copper mold, and they were dried by an electric oven with a sealed autoclave at 60 °C for 24 h. At last, through the total weight of the electrode and the weight ratio of MnCo$_2$O$_4$/ATB/PTFE (7:2:1), the weight of active material (MnCo$_2$O$_4$) in every disk electrode was calculated (2−3 mg).

The electrochemical performance of the MnCo$_2$O$_4$ disk electrodes was evaluated by coin cells with lithium metal as the reference electrode. In addition, the electrolyte solution is 1 mol·L^{-1} LiPF$_6$ dissolved in the mixture of ethylene carbonate (EC), propylene carbonate (PC), and diethyl carbonate (DEC) with a volume ratio of EC/PC/DEC = 3:1:1. The galvanostatic discharge/charge capacity was performed by the electrochemical test instrument (Land, CT2001A) at 25 °C, and the cyclic voltammogram (CV) curve was measured by an electrochemical workstation (Princeton, Parstat2273) at a scan rate of 0.1 mV·s^{-1} in the range of 0.01−3.00 V (vs. Li$^+$/Li).
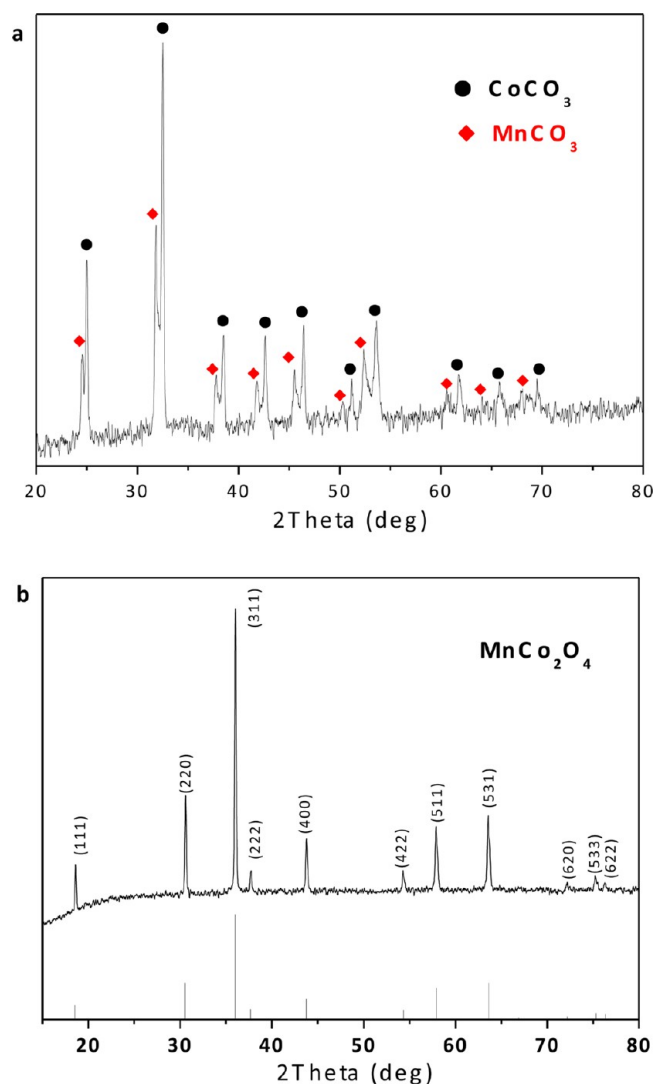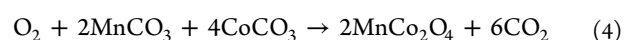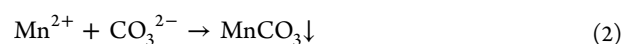
Figure 1. XRD patterns of samples. (a) Precursor and (b) $MnCo_2O_4$.

RESULTS AND DISCUSSION

Scheme 1 illustrates the preparation of the core−shell ellipsoidal $MnCo_2O_4$ with the desired concentration gradient and micro/nano-structure. Under the appropriate hydrothermal condition and the influence of special weak alkaline surfactant (triethanolamine, TEA), the $CoCO_3$ and $MnCO_3$ precursor is anticipated to grow to a well-defined microscale ellipsoid. During the reaction [eq 1], the hydrolysis of $CO(NH_2)_2$ slowly increases the pH of the reaction system, leading to different precipitation rates of $CoCO_3$ and $MnCO_3$ [eqs 2 and 3, respectively] and hence the concentration gradient in the precursor (mixture of $CoCO_3$ and $MnCO_3$). The decomposition and release of CO_2 [eq 4] by the thermal treatment converts the precursor to nanostructured, porous $MnCo_2O_4$ microparticles,[35,37] with an inherited concentration gradient controlled by the differential precipitation rates of $CoCO_3$ and $MnCO_3$.[40−44]

$$CO(NH_2)_2 + 2H_2O \rightarrow 2NH_4^+ + CO_3^{2-} \qquad (1)$$

$$Mn^{2+} + CO_3^{2-} \rightarrow MnCO_3\downarrow \qquad (2)$$

$$Co^{2+} + CO_3^{2-} \rightarrow CoCO_3\downarrow \qquad (3)$$

$$O_2 + 2MnCO_3 + 4CoCO_3 \rightarrow 2MnCo_2O_4 + 6CO_2 \qquad (4)$$

The X-ray powder diffraction (XRD) patterns of the samples are shown in Figure 1. The diffraction patterns of the precursor are indexed as a mixture of hexagonal $CoCO_3$ (JCPDS no. 78-0209) and hexagonal $MnCO_3$ (JCPDS no. 85-1109) (Figure 1a). After thermal treatment, the diffraction patterns of the final product agree well with the standard diffraction patterns of cubic phase $MnCo_2O_4$ (JCPDS no. 23-1237), exhibiting good crystallinity and purity (Figure 1b), and the specific surface areas of precursor and product are determined to be about 0.90 m^2g^{-1} and 53.00 m^2g^{-1}, respectively (Figure S1, Supporting Information). The scanning electron microscope (SEM) and transmission electron microscope (TEM) micrographs of the precursor in Figure 2 indicate that the precursor is of a regular monodispersed ellipsoidal shape with the long and short axis of
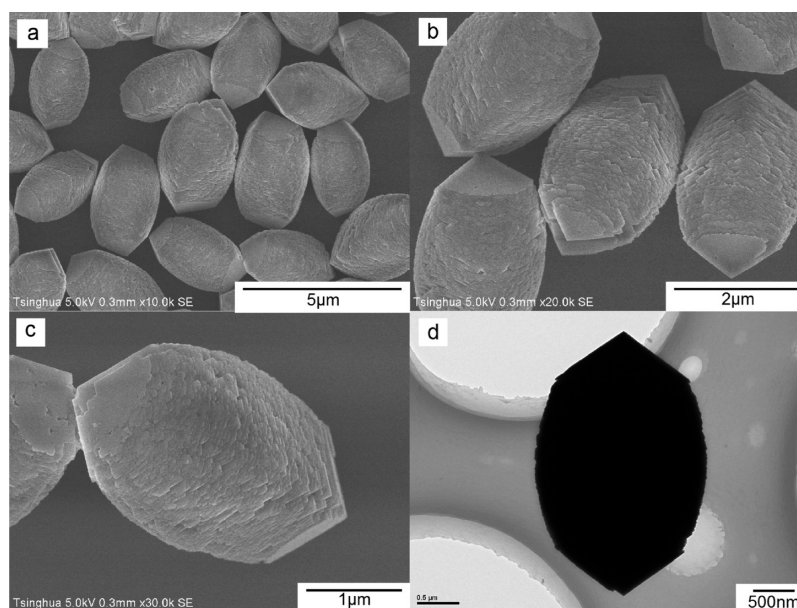

Figure 2. (a−c) SEM and (d) TEM images of the $CoCO_3$ and $MnCO_3$ precursor.
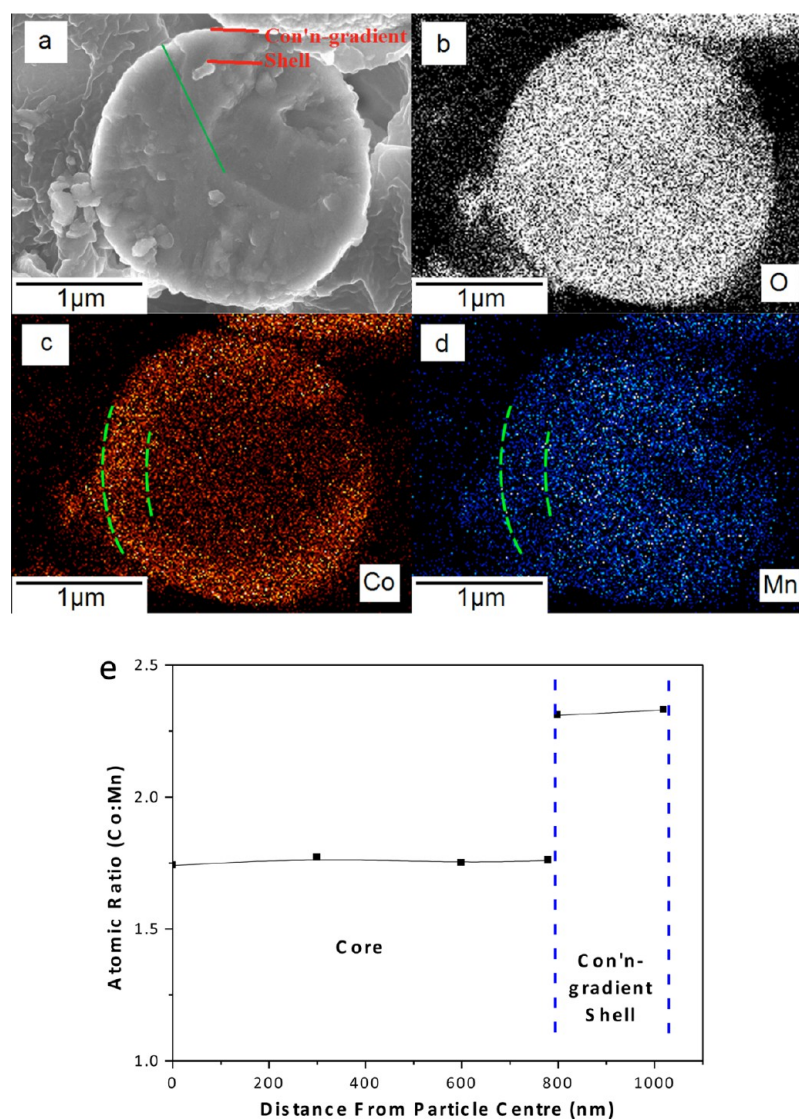
Figure 3. (a) SEM image and (b−d) the corresponding EDX mapping images of the ellipsoidal precursor's cross section. (e) Atomic ratio (Co/Mn) as a function of the distance from the particle center to the edge of the corresponding line in (a).

2.5−4.5 and 1.5−2.5 μm, respectively (Figure 2a,b). Interestingly, the morphology of the SEM micrographs indicates that the ellipsoid may be formed by numerous superimposed sheets, similar to the structure obtained in our previous report (Figure 2c).[37] The TEM micrograph (Figure 2d) clearly shows the ellipsoidal shape of the precursor particle.

The SEM micrograph and the corresponding energy dispersive X-ray (EDX) mapping images of the cross-section of the precursor ellipsoid are shown in Figures 3a−d. The EDX mapping image of Figure 3c clearly indicates that the concentration of Co in the shell (the thickness of 200−300 nm) is higher than in the core. In contrast, the Mn concentration in the shell is lower than in the core (Figure 3d). Furthermore, in Figure 3e, the curve of atomic ratio (Co/Mn) versus the distance from the particle center to the edge of the corresponding line in Figure 3a confirms the observation of Co and Mn EDX mapping results shown in Figure 3c,d that the precursor ellipsoid possesses shell to core concentration gradient, and the representative EDX spectra (Figure S2a,b, Supporting Information) show an increase in the Co/Mn atomic ratio from 1.75:1 for the core to 2.31:1 for the shell.

The SEM micrographs of the produced $MnCo_2O_4$ in Figure 4a,b show regular ellipsoidal shape and porous structure, similar to the morphology and size of the corresponding precursor. The SEM micrographs of the $MnCo_2O_4$ ellipsoids with broken shells (Figure S3, Supporting Information) clearly show that all the ellipsoids exhibit core−shell structure (the size of the shell is much smaller than the size of the core). All the microscale ellipsoids are built up by irregular nanoparticles attached to each other (Figure S4, Supporting Information).[35,37] The core−shell structure of the synthesized $MnCo_2O_4$ ellipsoid is further shown in the corresponding TEM micrograph (Figure 4c). The high resolution TEM micrograph in Figure 4d shows a 250 nm thickness of the shell. As shown by the SAED pattern in Figure 4e, the synthesized $MnCo_2O_4$ ellipsoid is polycrystalline with clear diffraction rings, which can be indexed to (220), (311), (400), (422), and (551) planes, respectively. These diffraction patterns are consistent with the XRD pattern shown in Figure 1b. The lattice fringes with lattice spacings of 0.48 and 0.25 nm agree well with the (111) and (311) crystal planes of cubic phase $MnCo_2O_4$ shown by the high-resolution trans-
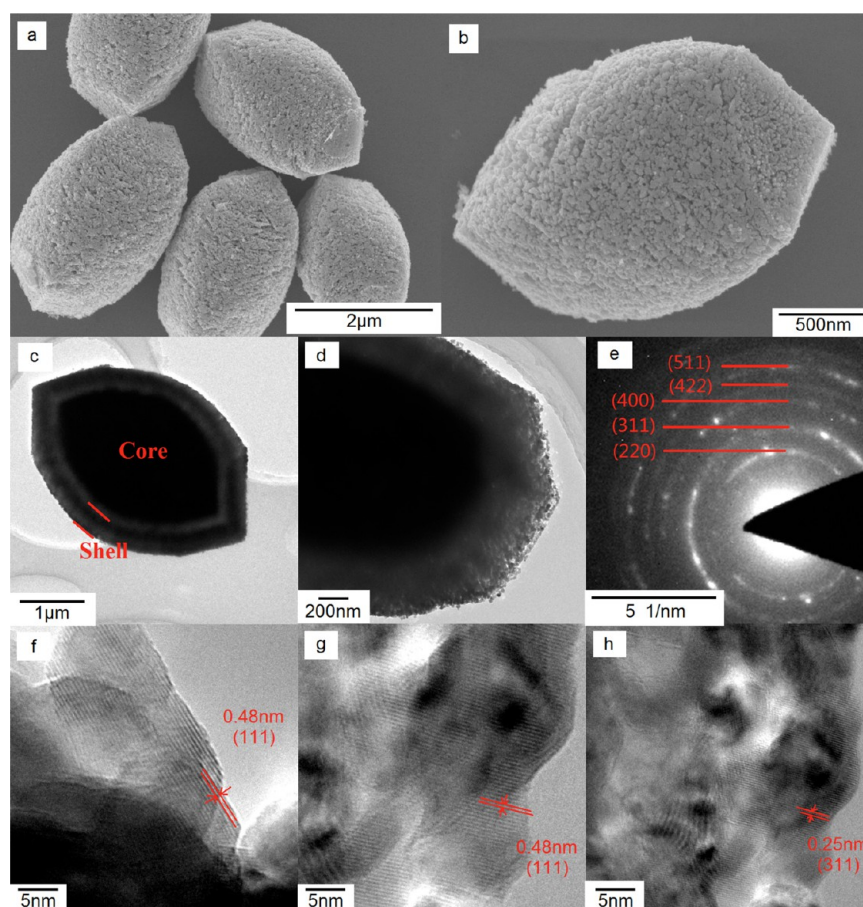
21328

dx.doi.org/10.1021/am506292b | ACS Appl. Mater. Interfaces 2014, 6, 21325−21334

Figure 4. (a, b) SEM images, (c, d) TEM images, (e) SEAD pattern, and (f–h) HRTEM images of MnCo₂O₄ powders.
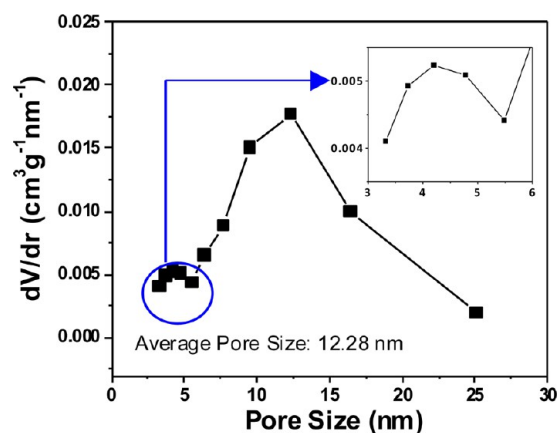

Figure 5. BJH pore-size distribution of MnCo₂O₄ powders. The inset is the partially enlarged detail of the corresponding location.

mission electron microscope (HRTEM) micrographs (Figure 4f–h).

The data obtained from the nitrogen adsorption/desorption isotherm (Figure S5, Supporting Information) are used to calculate the pore-size distribution of MnCo₂O₄ powders. The results in Figure 5 show an average pore size of about 12.5 nm. Interestingly, the results appear to show a bimodal pore distribution of the sample. The smaller pore size of lower intensity peak (partially enlarged in the inset of Figure 5) may represent the pore size distribution of the shell (3.3−5.5 nm), and the other relatively larger pore size and stronger intensity

peak matches well with the pore size distribution of the core (5.5−25.0 nm).

The SEM micrograph and the corresponding EDX mapping images of the cross-section of the synthesized porous MnCo₂O₄ ellipsoid are shown in Figure 6a−d. As in the case of its precursors, the Mn concentration (Figure 6d) is much lower in the shell than in the core. Furthermore, in Figure 6e, the curve of the atomic ratio (Co/Mn) versus the distance from the particle center to the edge of the corresponding line in Figure 6a shows that the MnCo₂O₄ ellipsoid also possesses a similar shell to core concentration gradient (the representative EDX spectra in Figure S6a,b, Supporting Information, show an increase in the Co/Mn atomic ratio from 1.76:1 for the core to 2.34:1 for the shell). Interestingly, this concentration value is close to the value of its precursor, indicating minimal change in chemical composition and microreaction of ions from the core to shell during the thermal treatment. In addition, a striking feature of the SEM micrograph (Figure 6a) is the presence of a crack separating the core from the shell of distinct chemical compositions (Figures 6b−d). This crack may be formed as a result of uneven chemical composition and stress distribution during thermal conversion of the precursors.

The electrochemical performance of the synthesized MnCo₂O₄ was evaluated by coin cells with lithium metal as the reference electrode. The first four cyclic voltammogram (CV) curves of the MnCo₂O₄ anode were recorded at the scanning rate of 0.1 mV·s⁻¹ over the voltage range of 0.01−3.00 V (vs. Li⁺/Li) in Figure 7a. The CV curve of the first cycle shows two well-defined reduction peaks at 0.97 and 0.25 V,
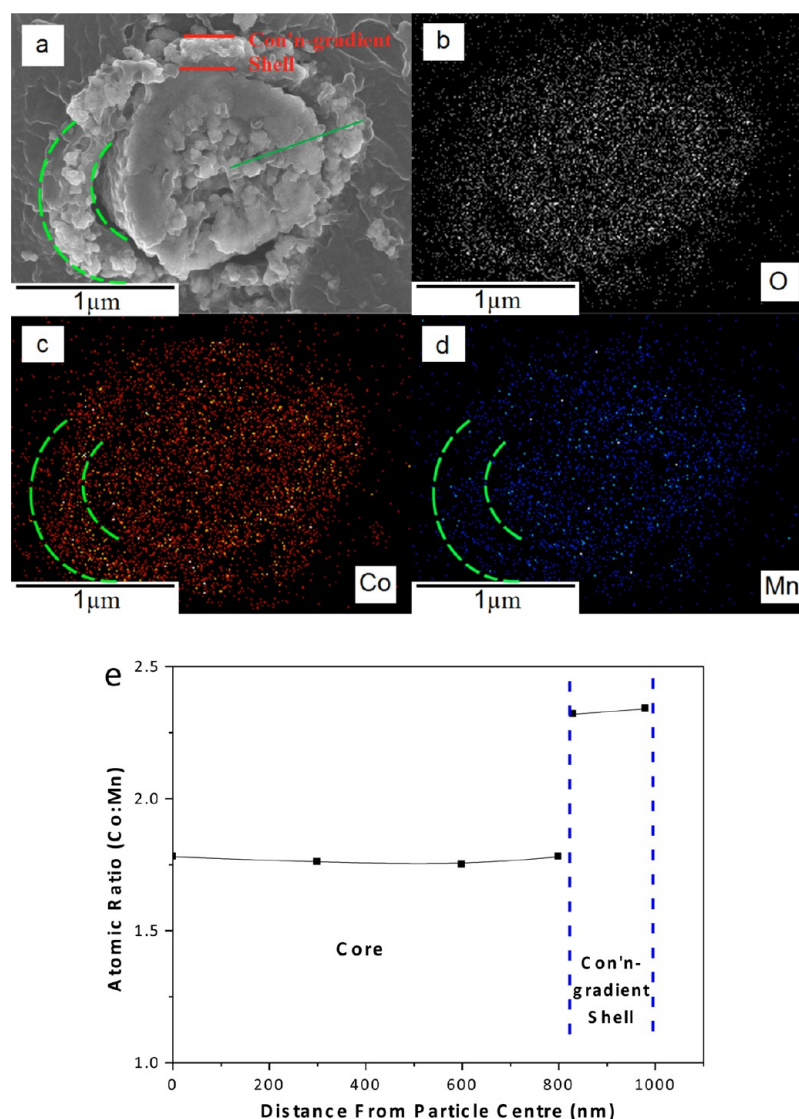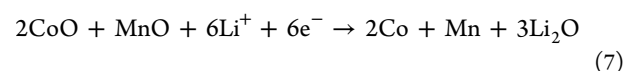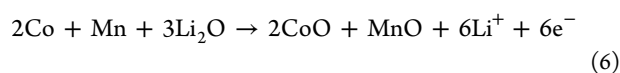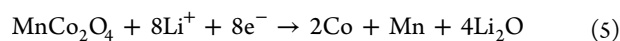
21329

dx.doi.org/10.1021/am506292b | ACS Appl. Mater. Interfaces 2014, 6, 21325−21334

Figure 6. (a) SEM image and (b−d) the corresponding EDX mapping images of the cross section of the MnCo$_2$O$_4$ ellipsoid. (e) Atomic ratio (Co/Mn) as a function of the distance from the particle center to the edge of the corresponding line in (a).

corresponding to the reductions of Co^{3+} to Co^{2+} and Co^{2+} and Mn^{2+} to metallic Co and Mn, respectively [eq 5].[26,37,39] Also evident is an anodic peak at 2.09 V, which could arise from the oxidation of Me to MeO (Me = Co, Mn) [eq 6].[31] In the subsequent cycles, only one reduction peak at ~0.85 V is observed, which may correspond to the other reduction reaction of MeO to Me (Me = Co, Mn) [eq 7]. A similar oxidation peak at ~2.27 V is observed, which is attributed to the same oxidation reaction [eq 6].[31,37] It is evident that the electrochemical reaction is fully reversible after the first cycle. In addition, compared with the intensity of the reduction peak at the first cycle, it decreases at the second to fourth cycle due to the irreversible reduction reaction as other single or binary metal oxides and the formation of the irreversible solid electrolyte interface (SEI) film.[21,37,45]

$$MnCo_2O_4 + 8Li^+ + 8e^- \rightarrow 2Co + Mn + 4Li_2O \qquad (5)$$

$$2Co + Mn + 3Li_2O \rightarrow 2CoO + MnO + 6Li^+ + 6e^- \qquad (6)$$

$$2CoO + MnO + 6Li^+ + 6e^- \rightarrow 2Co + Mn + 3Li_2O \qquad (7)$$

The discharge/charge curves of the MnCo$_2$O$_4$ anode in the voltage range of 0.01−3.00 V (vs. Li$^+$/Li) at 0.1 Ag^{-1} are shown in Figure 7b. The initial discharge and charge capacities are 1433.3 and 845.9 mAhg^{-1}, respectively. Such discharge/charge characteristics correspond to an irreversible capacity loss ratio of about 40%, which is typical for such type of anodes and may arise from the formation of an irreversible SEI film during the first discharge cycle.[37,39,46] In the subsequent cycles, the discharge/charge profiles tend to be stable and exhibit a similar electrochemical behavior with approximate discharge and charge capacities of 900.0 and 850.0 mAhg^{-1}. Interestingly, these capacities are higher than the theoretical total capacity of MnCo$_2$O$_4$ (691.0 mAhg^{-1}). There are two possible reasons contributing to the additional reversible capacity: (1) the reversible side reactions of Mn^{2+} to Mn^{3+} or even to Mn^{4+};[39,47] and (2) the reversible formation/dissolution of the polymer/gel-like film.[31,32]
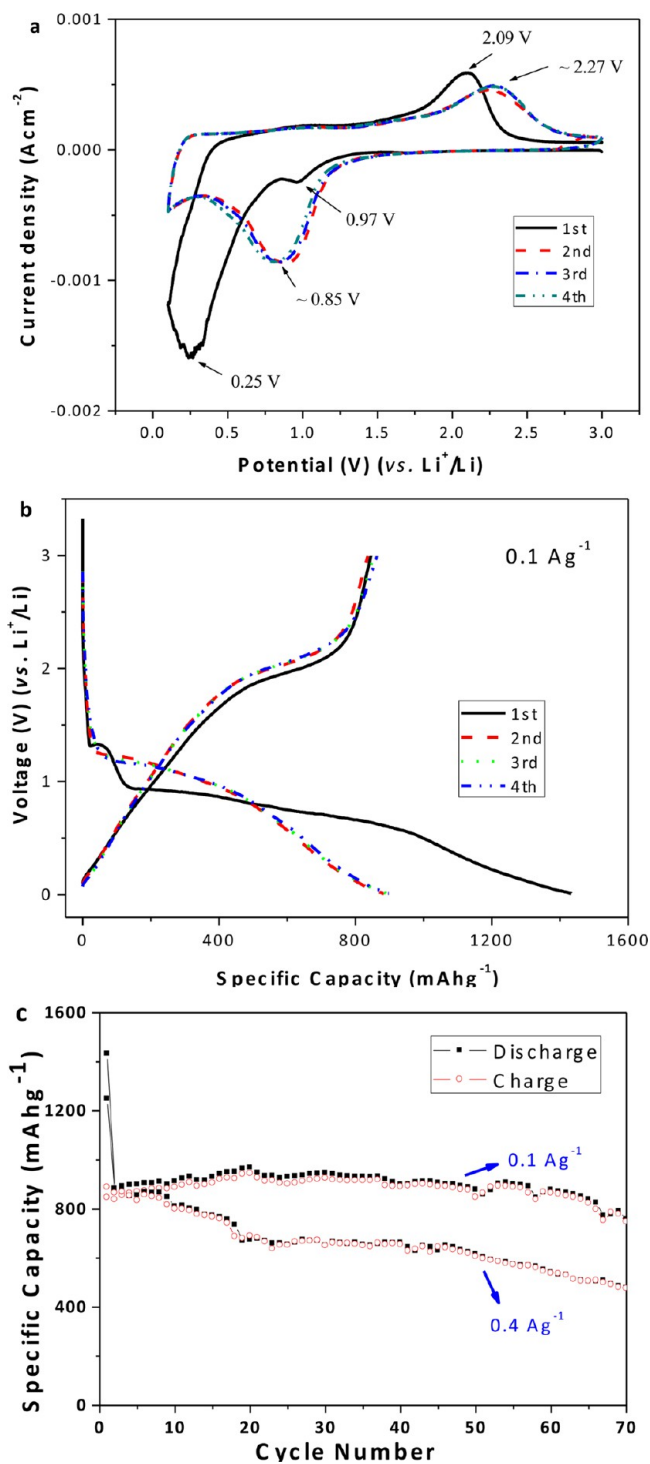
Figure 8. SEM images of the $MnCo_2O_4$ electrode (mixture of $MnCo_2O_4$/ATB/PVDF) after 70 cycles during 0.1 Ag^{-1} at different magnifications. (a) 5000 and (b) 30 000.

Figure 7. (a) First to the fourth CV curves of the $MnCo_2O_4$ electrode at a scan rate of 0.1 mV·s^{-1} in the range of 0.01–3.00 V. (b) Discharge and charge profiles of the $MnCo_2O_4$ electrode in the range of 0.01–3.00 V at 0.1 Ag^{-1}. (c) Cycling performance of the $MnCo_2O_4$ electrodes at 0.1 and 0.4 Ag^{-1}.

The cycling performance of $MnCo_2O_4$ anodes at 0.1 and 0.4 Ag^{-1} with 70 cycles is shown in Figure 7c. At the low current density of 0.1 Ag^{-1}, the reversible capacity from the 2nd cycle to the 25th cycle increases slowly and gradually from ~850.0 to ~950.0 $mAhg^{-1}$, which may be caused by the Li-ion diffusion being stabilized and activated gradually during the discharge/charge process.[48,49] From the 26th cycle up to the 60th cycle,
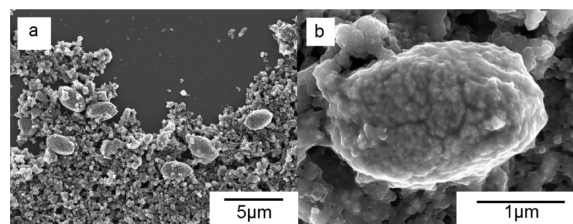
the reversible capacity remains at a high value between 900.0 and 950.0 $mAhg^{-1}$. Further prolonged discharge/charge cycling led to a slight decrease in the reversible capacity to ~750 $mAhg^{-1}$ at the 70th cycle. In comparison, at the high current density of 0.4 Ag^{-1}, the initial discharge and charge capacities are lower at 1248.4 and 888.3 $mAhg^{-1}$, respectively. The discharge capacity stayed at a high value between 870.0 and 820.0 $mAhg^{-1}$ from the second cycle to the 12th cycle. Similarly to the low current density case, the reversible capacity goes down slowly to ~620.0 $mAhg^{-1}$ at the 50th cycle, corresponding to a capacity retention ratio (versus the second discharge capacity) of about 74.0%, and further discharge/charge cycling from the 50th cycle to the 70th cycle led to a steady decrease in the reversible capacity. These results clearly illustrate that the core–shell $MnCo_2O_4$ ellipsoids with micro/nano-structure and concentration gradient are of high initial discharge capacity, advanced capacity retention, and good rate performance. Basically, two possible reasons explain the good performance of such $MnCo_2O_4$ anode as follows. (1) The special structures of multipore and micro/nanoscale contribute to large specific surface area and promoting the electrolyte diffusion. (2) The stable cobalt-rich shell improves the stability of the lithiation/delithiation process.[41,43] There may be other important reasons for its good electrochemical performance.

To further understand the discharge and charge behaviors, the $MnCo_2O_4$ electrode (mixture of $MnCo_2O_4$/ATB/PVDF) after 70 cycles at 0.1 Ag^{-1} is investigated by SEM. The SEM micrographs in Figure 8 show that the $MnCo_2O_4$ remains ellipsoidal. Remarkably, the SEM micrograph of the vertical section of the $MnCo_2O_4$ ellipsoid after 70 cycles at 0.1 Ag^{-1} in Figure 9a shows a clear core–shell structure separated by the visible crack. The corresponding EDX mapping images of the Co element (Figure 9c) and Mn element (Figure 9d) confirm the relatively higher Co to Mn concentration ratio in the shell than that in the core, as also shown by the corresponding curve in Figure 9e. Quantitively, the Co/Mn atomic ratios of core and shell (Figure S7a,b, Supporting Information) are similar to the $MnCo_2O_4$ ellipsoid before the electrochemical reaction, confirming that the concentration gradient of the core–shell structure is still retained. Clearly, the concentration gradient may be the major contribution to the retention in the reversed capacity after long cycling.

■ CONCLUSIONS

In summary, through the hydrothermal method followed by thermal treatment, novel core–shell ellipsoidal $MnCo_2O_4$ powders with a desired micro/nano-structure and unique concentration gradient have been synthesized, which inherit the special morphology and structure of precursor (mixture of $CoCO_3$ and $MnCO_3$). The porous core–shell ellipsoid (2.5–4.5 μm in the long axis, 1.5–2.5 μm in the short axis, 200–300
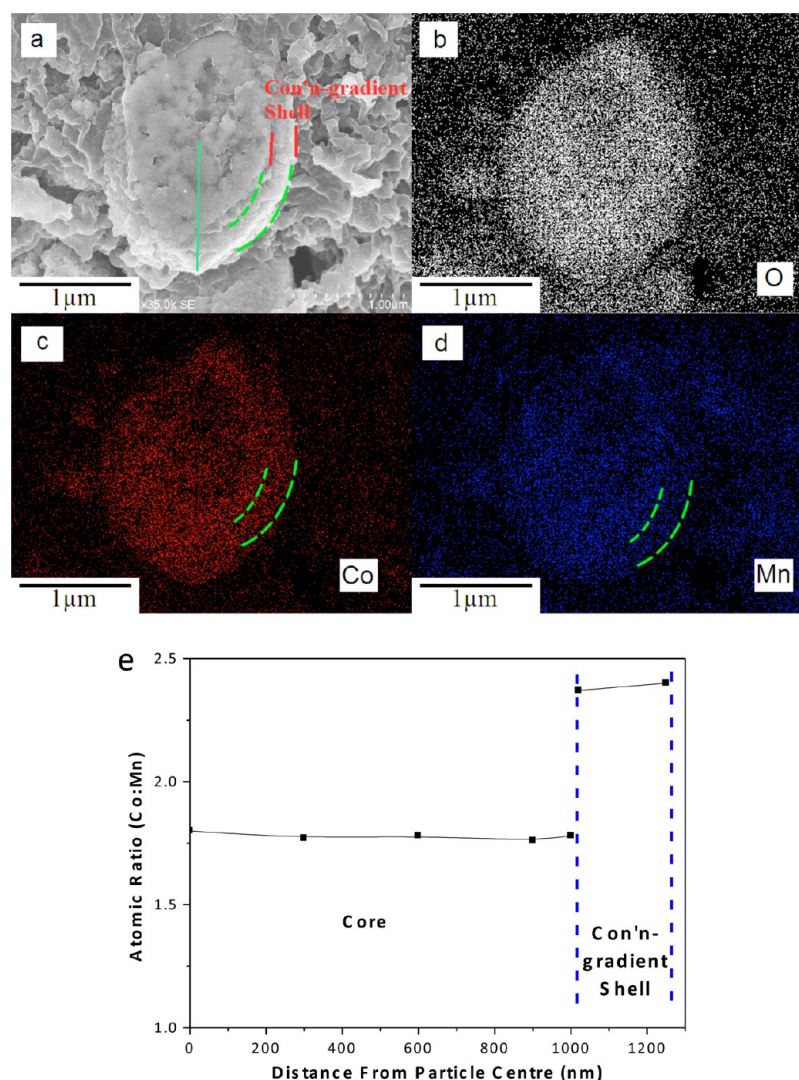
Figure 9. (a) SEM image and (b−d) the corresponding EDX mapping images of the vertical section of the MnCo$_2$O$_4$ ellipsoid after 70 cycles at 0.1 Ag^{-1}. (e) Atomic ratio (Co/Mn) as a function of the distance from the particle center to the edge of the corresponding line in (a).

nm in the thickness of the shell) is built up by irregular nanoparticles attached to each other. The specific surface area is 53.00 m^{2}g^{-1}, and the pore size of the shell (~4.3 nm, average) is much smaller than that of the core (~12.5 nm, average). In addition, corresponding to the ellipsoid with concentration gradient, the Co/Mn atomic ratios of core and shell are about 1.76:1 and 2.34:1, respectively. Evaluated by electrochemical measurements, the good performance has been proved including high initial discharge capacities (1433.3 mAhg^{-1} at 0.1 Ag^{-1} and 1248.4 mAhg^{-1} at 0.4 Ag^{-1}), advanced capacity retention (~900.0 mAhg^{-1} after 60 cycles at 0.1 Ag^{-1}), and fair rate performance (~620.0 mAhg^{-1} after 50 cycles at 0.4 Ag^{-1}). Remarkably, the ellipsoidal shape and core−shell microstructure with the concentration gradient are still retained after 70 cycles at 0.1 Ag^{-1}. The unique morphology and special structures may be extended to synthesize other binary transition metal oxides.

ASSOCIATED CONTENT

Ⓢ Supporting Information

N$_2$ adsorption isotherms of the precursor and MnCo$_2$O$_4$ powders. Representative EDX spectra in Figures 3a, 6a, and 9a. SEM images of MnCo$_2$O$_4$ ellipsoid. N$_2$ adsorption/ desorption isotherms of MnCo$_2$O$_4$ powders. This material is available free of charge via the Internet at http://pubs.acs.org.

AUTHOR INFORMATION

Corresponding Authors

*E-mail: smxu@tsinghua.edu.cn.
*E-mail: zhenghe.xu@ualberta.ca.

Notes

The authors declare no competing financial interest.

REFERENCES

(1) Kang, K.; Meng, Y. S.; Breger, J.; Grey, C. P.; Ceder, G. Electrodes with High Power and High Capacity for Rechargeable Lithium Batteries. *Science* **2006**, *311*, 977−980.
(2) Dunn, B.; Kamath, H.; Tarascon, J. M. Electrical Energy Storage for the Grid: A Battery of Choices. *Science* **2011**, *334*, 928−935.

(3) Simon, P.; Gogotsi, Y. Materials for Electrochemical Capacitors. *Nat. Mater.* **2008**, *7*, 845−854.

(4) Goodenough, J. B.; Park, K. S. The Li-Ion Rechargeable Battery: A Perspective. *J. Am. Chem. Soc.* **2013**, *135*, 1167−1176.

(5) Yang, L.; Cheng, S.; Ding, Y.; Zhu, X.; Wang, Z. L.; Liu, M. Hierarchical Network Architectures of Carbon Fiber Paper Supported Cobalt Oxide Nanonet for High-Capacity Pseudocapacitors. *Nano Lett.* **2012**, *12*, 321−325.

(6) Wei, T. Y.; Chen, C. H.; Chien, H. C.; Lu, S. Y.; Hu, C. C. A Cost-Effective Supercapacitor Material of Ultrahigh Specific Capacitances: Spinel Nickel Cobaltite Aerogels from an Epoxide-Driven Sol-Gel Process. *Adv. Mater.* **2010**, *22*, 347−351.

(7) Sun, X.; Yan, C.; Chen, Y.; Si, W.; Deng, J.; Oswald, S.; Liu, L.; Schmidt, O. G. Three-Dimensionally "Curved" NiO Nanomembranes as Ultrahigh Rate Capability Anodes for Li-Ion Batteries with Long Cycle Lifetimes. *Adv. Energy Mater.* **2014**, *4* (1300912), 1−6.

(8) Ko, S.; Lee, J. I.; Yang, H. S.; Park, S.; Jeong, U. Mesoporous CuO Particles Threaded with CNTs for High-Performance Lithium-Ion Battery Anodes. *Adv. Mater.* **2012**, *24*, 4451−4456.

(9) Lee, J. W.; Hall, A. S.; Kim, J. D.; Mallouk, T. E. A Facile and Template-Free Hydrothermal Synthesis of Mn_3O_4 Nanorods on Graphene Sheets for Supercapacitor Electrodes with Long Cycle Stability. *Chem. Mater.* **2012**, *24*, 1158−1164.

(10) Subramanian, V.; Karki, A.; Gnanasekar, K. I.; Eddy, F. P.; Rambabu, B. Nanocrystalline TiO_2 (Anatase) for Li-Ion Batteries. *J. Power Sources* **2006**, *159*, 186−192.

(11) Eustache, E.; Tilmant, P.; Morgenroth, L.; Roussel, P.; Patriarche, G.; Troadec, D.; Rolland, N.; Brousse, T.; Lethien, C. Silicon-Microtube Scaffold Decorated with Anatase TiO_2 as a Negative Electrode for a 3D Litium-Ion Microbattery. *Adv. Energy Mater.* **2014**, *4* (1301612), 1−11.

(12) Wang, H.; Cui, L. F.; Yang, Y.; Casalongue, H. S.; Robinson, J. T.; Liang, Y.; Cui, Y.; Dai, H. Mn_3O_4-Graphene Hybrid as a High-Capacity Anode Material for Lithium Ion Batteries. *J. Am. Chem. Soc.* **2010**, *132*, 13978−13980.

(13) Dong, X. C.; Xu, H.; Wang, X. W.; Huang, Y. X.; Park, M. B. C.; Zhang, H.; Wang, L. H.; Huang, W.; Chen, P. 3D Graphene-Cobalt Oxide Electrode for High-Performance Supercapacitor and Enzymeless Glucose Detection. *ACS Nano* **2012**, *6*, 3206−3213.

(14) Poizot, P.; Laruelle, S.; Grugeon, S.; Dupont, L.; Tarascon, J. M. Nano-Sized Transition-Metal Oxides as Negative-Electrode Materials for Lithium-Ion Batteries. *Nature* **2000**, *407*, 496−499.

(15) Song, M. K.; Cheng, S.; Chen, H.; Qin, W.; Nam, K. W.; Xu, S.; Yang, X. Q.; Bongiorno, A.; Lee, J.; Bai, J.; Tyson, T. A.; Cho, J.; Liu, M. Anomalous Pseudocapacitive Behavior of a Nanostructured, Mixed-Valent Manganese Oxide Film for Electrical Energy Storage. *Nano Lett.* **2012**, *12*, 3483−3490.

(16) Chen, S. Q.; Wang, Y. Microwave-Assisted Synthesis of a Co_3O_4-Graphene Sheet-on-Sheet Nanocomposite as a Superior Anode Material for Li-Ion Batteries. *J. Mater. Chem.* **2010**, *20*, 9735−9739.

(17) Xia, X.; Tu, J.; Zhang, Y.; Wang, X.; Gu, C.; Zhao, X. B.; Fan, H. J. High-Quality Metal Oxide Core/Shell Nanowire Arrays on Conductive Substrates for Electrochemical Energy Storage. *ACS Nano* **2012**, *6*, 5531−5538.

(18) Cui, B.; Lin, H.; Li, J. B.; Li, X.; Yang, J.; Tao, J. Core-Ring Structured $NiCo_2O_4$ Nanoplatelets: Synthesis, Characterization, and Electrocatalytic Applications. *Adv. Funct. Mater.* **2008**, *18*, 1440−1447.

(19) Zhang, G.; Lou, X. W. General Solution Growth of Mesoporous $NiCo_2O_4$ Nanosheets on Various Conductive Substrates as High-Performance Electrodes for Supercapacitors. *Adv. Mater.* **2013**, *25*, 976−979.

(20) Cherian, C. T.; Sundaramurthy, J.; Reddy, M. V.; Kumar, P. S.; Mani, K.; Pliszka, D.; Sow, C. H.; Ramakrishna, S.; Chowdari, B. V. R. Morphologically Robust $NiFe_2O_4$ Nanofibers as High Capacity Li-Ion Battery Anode Material. *ACS Appl. Mater. Interfaces* **2013**, *5*, 9957−9963.

(21) Wang, Y.; Su, D.; Ung, A.; Ahn, J. H.; Wang, G. Hollow $CoFe_2O_4$ Nanospheres as a High Capacity Anode Material for Lithium Ion Batteries. *Nanotechnology* **2012**, *23* (055402), 1−6.

(22) Sharma, Y.; Sharma, N.; Rao, G. V. S.; Chowdari, B. V. R. Nanophase $ZnCo_2O_4$ as a High Performance Anode Material for Li-Ion Batteries. *Adv. Funct. Mater.* **2007**, *17*, 2855−2861.

(23) Li, J.; Wang, J.; Wexler, D.; Shi, D.; Liang, J.; Liu, H.; Xiong, S.; Qian, Y. Simple Synthesis of Yolk-Shelled $ZnCo_2O_4$ Microspheres towards Enhancing the Electrochemical Performance of Lithium-Ion Batteries in Conjunction with a Sodium Carboxymethyl Cellulose Binder. *J. Mater. Chem. A* **2013**, *1*, 15292−15299.

(24) Lavela, P.; Tirado, J. L.; Abarca, V. C. Sol-Gel Preparation of Cobalt Manganese Mixed Oxides for their Use as Electrode Materials in Lithium Cells. *Electrochim. Acta* **2007**, *52*, 7986−7995.

(25) Padmanathan, N.; Selladurai, S. Mesoporous $MnCo_2O_4$ Spinel Oxide Nanostructure Synthesized by Solvothermal Technique for Supercapacitor. *Ionics* **2014**, *20*, 479−487.

(26) Hu, L.; Zhong, H.; Zheng, X.; Huang, Y.; Zhang, P.; Chen, Q. $CoMn_2O_4$ Spinel Hierarchical Microspheres Assembled with Porous Nanosheets as Stable Anodes for Lithium-Ion Batteries. *Sci. Rep.* **2012**, *2* (986), 1−8.

(27) Chen, S.; Qiao, S. Z. Hierarchically Porous Nitrogen-Doped Graphene/$NiCo_2O_4$ Hybrid Paper as an Advanced Electrocatalytic Water-Splitting Material. *ACS Nano* **2013**, *7*, 10190−10196.

(28) Huang, L.; Chen, D.; Ding, Y.; Feng, S.; Wang, Z. L.; Liu, M. Nickel-Cobalt Hydroxide Nanosheets Coated on $NiCo_2O_4$ Nanowires Grown on Carbon Fiber Paper for High-Performance Pseudocapacitors. *Nano Lett.* **2013**, *13*, 3135−3139.

(29) Courtel, F. M.; Duncan, H.; Lebdeh, Y. A.; Davidson, I. J. High Capacity Anode Materials for Li-Ion Batteries Based on Spinel Metal Oxides AMn_2O_4 (A = Co, Ni, and Zn). *J. Mater. Chem.* **2011**, *21*, 10206−10218.

(30) Paudel, T. R.; Zakutayev, A.; Lany, S.; Avezac, M. D.; Zunger, A. Doping Rules and Doping Prototypes in A_2BO_4 Spinel Oxides. *Adv. Funct. Mater.* **2011**, *21*, 4493−4501.

(31) Li, J.; Xiong, S.; Li, X.; Qian, Y. A Facile Route to Synthesize Multiporous $MnCo_2O_4$ and $CoMn_2O_4$ Spinel Quasi-Hollow Spheres with Improved Lithium Storage Properties. *Nanoscale* **2013**, *5*, 2045−2054.

(32) Li, J.; Wang, J.; Liang, X.; Zhang, Z.; Liu, H.; Qian, Y.; Xiong, S. Hollow $MnCo_2O_4$ Submicrospheres with Multilevel Interiors: From Mesoporous Spheres to Yolk-in-Double-Shell Structures. *ACS Appl. Mater. Interfaces* **2014**, *6*, 24−30.

(33) Li, L.; Zhang, Y. Q.; Liu, X. Y.; Shi, S. J.; Zhao, X. Y.; Zhang, H.; Ge, X.; Cai, G. F.; Gu, C. D.; Wang, X. L.; Tu, J. P. One-Dimension $MnCo_2O_4$ Nanowire Arrays for Electrochemical Energy Storage. *Electrochim. Acta* **2014**, *116*, 467−474.

(34) Hu, L.; Wu, L.; Liao, M.; Hu, X.; Fang, X. Electrical Transport Properties of Large, Individual $NiCo_2O_4$ Nanoplates. *Adv. Funct. Mater.* **2012**, *22*, 998−1004.

(35) Huang, G. Y.; Xu, S. M.; Lu, S. S.; Li, L. Y.; Sun, H. Y. Porous Polyhedral and Fusiform Co_3O_4 Anode Materials for High-Performance Lithium-Ion Batteries. *Electrochim. Acta* **2014**, *135*, 420−427.

(36) Wang, L.; Liu, B.; Ran, S.; Wang, L.; Gao, L.; Qu, F.; Chen, D.; Shen, G. Facile Synthesis and Electrochemical Properties of $CoMn_2O_4$ Anodes for High Capacity Lithium-Ion Batteries. *J. Mater. Chem. A* **2013**, *1*, 2139−2143.

(37) Huang, G. Y.; Xu, S. M.; Lu, S. S.; Li, L. Y.; Sun, H. Y. Micro-/Nano-Structured Co_3O_4 Anode with Enhanced Rate Capability for Lithium-Ion Batteries. *ACS Appl. Mater. Interfaces* **2014**, *6*, 7236−7243.

(38) Reddy, M. V.; Yu, C.; Fan, J.; Loh, K. P.; Chowdari, B. V. R. Li-Cycling Properties of Molten Salt Method Prepared Nano/Submicrometer and Micrometer-Sized CuO for Lithium Batteries. *ACS Appl. Mater. Interfaces* **2013**, *5*, 4361−4366.

(39) Yu, L.; Zhang, L.; Wu, H. B.; Zhang, G.; Lou, X. W. Controlled Synthesis of Hierarchical $Co_xMn_{3-x}O_4$ Array Micro-/Nanostructures with Tunable Morphology and Composition as Integrated Electrodes for Lithium-Ion Batteries. *Energy Environ. Sci.* **2013**, *6*, 2664−2671.

(40) Zhou, J.; Danilov, D.; Notten, P. H. L. A Novel Method for the In Situ Determination of Concentration Gradients in the Electrolyte of Li-Ion Batteries. *Chem.—Eur. J.* **2006**, *12*, 7125−7132.

21333

dx.doi.org/10.1021/am506292b | *ACS Appl. Mater. Interfaces* 2014, 6, 21325−21334

(41) Sun, Y. K.; Lee, B. R.; Noh, H. J.; Wu, H.; Myung, S. T.; Amine, K. A Novel Concentration-Gradient Li[Ni$_{0.83}$Co$_{0.07}$Mn$_{0.10}$]O$_2$ Cathode Material for High-Energy Lithium-Ion Batteries. *J. Mater. Chem.* **2011**, *21*, 10108−10112.

(42) Yang, X.; Wang, X.; Zou, G.; Hu, L.; Shu, H.; Yang, S.; Liu, L.; Hu, H.; Yuan, H.; Hu, B.; Wei, Q.; Yi, L. Spherical Lithium-Rich Layered Li$_{1.13}$[Mn$_{0.534}$Ni$_{0.233}$Co$_{0.233}$]$_{0.87}$O$_2$ with Concentration-Gradient Outer Layer as High-Performance Cathodes for Lithium Ion Batteries. *J. Power Sources* **2013**, *232*, 338−347.

(43) Sun, Y. K.; Kim, D. H.; Yoon, C. S.; Myung, S. T.; Prakash, J.; Amine, K. A Novel Cathode Material with a Concentration-Gradient for High-Energy and Safe Lithium-Ion Batteries. *Adv. Funct. Mater.* **2010**, *20*, 485−491.

(44) Jung, S. K.; Gwon, H.; Hong, J.; Park, K. Y.; Seo, D. H.; Kim, H.; Hyun, J.; Yang, W.; Kang, K. Understanding the Degradation Mechanisms of LiNi$_{0.5}$Co$_{0.2}$Mn$_{0.3}$O$_2$ Cathode Material in Lithium Ion Batteries. *Adv. Energy Mater.* **2014**, *4* (1300787), 1−7.

(45) Zhang, R.; Shen, D.; Xu, M.; Feng, D.; Li, W.; Zheng, G.; Che, R.; Elzatahry, A. A.; Zhao, D. Ordered Macro-/Mesoporous Anatase Films with High Thermal Stability and Crystallinity for Photo-electrocatalytic Water-Splitting. *Adv. Energy Mater.* **2014**, *4* (1301725), 1−7.

(46) Bai, S.; Cao, M.; Jin, Y.; Dai, X.; Liang, X.; Ye, Z.; Li, M.; Cheng, J.; Xiao, X.; Wu, Z.; Xia, Z.; Sun, B.; Wang, E.; Mo, Y.; Gao, F.; Zhang, F. Low-Temperature Combustion-Synthesized Nickel Oxide Thin Films as Hole-Transport Interlayers for Solution-Processed Optoelec-tronic Devices. *Adv. Energy Mater.* **2014**, *4* (1301460), 1−6.

(47) Arun, P. S.; Ranjith, B. P.; Shibli, S. M. A. Control of Carbon Monoxide (CO) from Automobile Exhaust by a Dealuminated Zeolite Supported Regenerative MnCo$_2$O$_4$ Catalyst. *Environ. Sci. Technol.* **2013**, *47*, 2746−2753.

(48) Yang, W.; Gao, Z.; Ma, J.; Zhang, X.; Wang, J.; Liu, J. Hierarchical NiCo$_2$O$_4$@NiO Core-Shell Heterostructured Nanowire Arrays on Carbon Cloth for a High-Performance Flexible All-Solid-State Electrochemical Capacitor. *J. Mater. Chem. A* **2014**, *2*, 144−1457.

(49) Liu, X.; Shi, S.; Xiong, Q.; Li, L.; Zhang, Y.; Tang, H.; Gu, C.; Wang, X.; Tu, J. Hierarchical NiCo$_2$O$_4$@NiCo$_2$O$_4$ Core/Shell Nanoflake Arrays as High-Performance Supercapacitor Materials. *ACS Appl. Mater. Interfaces* **2013**, *5*, 8790−8795.